Materials Research Express

PAPER • **OPEN ACCESS**

Magneto-structural properties of Mg-substituted copper ferrite nanoparticles

To cite this article: J Mazurenko *et al* 2024 *Mater. Res. Express* **11** 125003

Materials Research Express

PAPER

Magneto-structural properties of Mg-substituted copper ferrite nanoparticles

J Mazurenko[1,2], Sijo A K[3], L Kaykan[4], J M Michalik[2], Ł Gondek[2], E Szostak[5], Żywczak A[6] and V Moklyak[4,7]

[1] Ivano-Frankivsk National Medical University, 2 Halytska Str., Ivano-Frankivsk, 76018, Ukraine
[2] Department Physics and Applied Computer Science, AGH University of Krakow, Al. Mickiewicza 30, Krakow, 30-059, Poland
[3] Department of Physics, Mary Matha Arts and Science College, Mananthavady, Kannur University, Kerala-670654, India
[4] G.V. Kurdyumov Institute for Metal Physics, N.A.S. of Ukraine, 36 Academician Vernadsky Boulevard, Kyiv, 03142, Ukraine
[5] Department of Chemistry, Jagiellonian University, Kraków, 30-387, Poland
[6] Academic Centre for Materials and Nanotechnology, AGH University of Krakow, Kraków, 30-059, Poland
[7] Ivano-Frankivsk National Technical University of Oil and Gas, 15 Karpatska Str., Ivano-Frankivsk, Ukraine

E-mail: yumazurenko@ifnmu.edu.ua

Keywords: ferrite, nanoparticles, superparamagnetism, mössbauer studies, spin canting

OPEN ACCESS

RECEIVED
10 October 2024

REVISED
26 November 2024

ACCEPTED FOR PUBLICATION
9 December 2024

PUBLISHED
17 December 2024

Abstract

This study explores the synthesis and characterization of magnesium-substituted copper ferrite ($Mg_xCu_{1-x}Fe_2O_4$, $0.0 \leqslant x \leqslant 1.0$) nanoparticles using the polymer-assisted sol–gel self-combustion method. The effects of magnesium substitution on the structural, elastic, and magnetic properties of the ferrites were systematically investigated. X-ray diffraction (XRD) analysis confirmed the formation of single-phase cubic spinel structures with particle sizes ranging from 8–21 nm. A slight increases in the lattice parameter was observed with higher magnesium content, attributed to the substitution of smaller Cu^{2+} ions with slightly larger Mg^{2+} ions. Fourier Transform Infrared (FTIR) spectroscopy and Mössbauer spectroscopy revealed the spinel structure and complex magnetic interactions between ferromagnetic and superparamagnetic phases. The spin canting was observed and found to vary significantly across compositions, with a maximum canting angle of 58.47°. This notable result highlights the important magnetic behavior of these materials. The saturation magnetization (M_S) varied across samples, with the $x = 0.6$ composition exhibiting optimal magnetic performance. Cation distribution analysis using XRD, Mössbauer spectroscopy, and magnetic measurements consistently showed the redistribution of cations between the tetrahedral (A) and octahedral (B) sites in the spinel structure. This research demonstrates the potential of magnesium-substituted copper ferrites for magnetic applications, with notable improvements in magnetic and structural properties due to cation substitution.

1. Introduction

Spinel ferrites have become a focal point of research due to their adjustable magnetic, electrical, and catalytic properties, which make them highly versatile for modern technological applications. These materials are commonly utilized in microwave technologies, sensors, catalytic processes, electromagnetic interference (EMI) shielding, and energy storage solutions [1]. Spinel ferrites (AB_2O_4) possess a unique crystal structure that can host various cations in both tetrahedral (A) and octahedral (B) sites, enabling the tuning of their magnetic and electrical properties. Among them, copper ferrite ($CuFe_2O_4$) has been the subject of extensive research due to its unique Jahn–Teller distortion in the copper ion and its transition from a cubic to a tetragonal structure, which directly influences its magnetic behavior [2].

Magnesium-substituted copper ferrites ($Cu_{1-x}Mg_xFe_2O_4$) offer a promising area of investigation, as the introduction of nonmagnetic magnesium ions significantly affects both the structural and magnetic properties of the material [3]. Magnesium substitution is expected to alter the cation distribution between the tetrahedral and octahedral sites within the spinel structure, which, in turn, modifies superexchange interactions between

Fe^{2+}-Fe^{3+} and Cu^{2+}-Fe^{3+} ions [4]. This alteration leads to variations in magnetic ordering, which can either enhance or suppress certain properties, including coercivity, remanence, and saturation magnetization. Additionally, the smaller ionic radius of magnesium compared to copper may reduce the lattice constant, impacting the overall crystal structure and density of the material [5].

Ferrite materials can be synthesized using various methods, each offering distinct advantages in terms of particle size control, crystallinity, purity, and magnetic properties. Common techniques include solid-state reaction, co-precipitation, hydrothermal synthesis, and sol–gel methods [6]. The solid-state reaction, often used for bulk ferrites, typically requires high temperatures and long reaction times, resulting in larger particle sizes and less control over cation distribution [7]. Co-precipitation is a straightforward route to nanoparticle production at lower temperatures, but it may lead to agglomeration and variability in particle size. Hydrothermal synthesis, while capable of producing high-quality crystals at lower temperatures, demands specialized equipment and extended reaction times [8].

Among these techniques, the sol–gel autocombustion method has gained prominence due to its ability to produce nanocrystalline ferrites with high phase purity and controlled particle size [9]. This method involves preparing a gel from metal precursors and a chelating agent, followed by an exothermic combustion reaction to form the ferrite material. The autocombustion process not only simplifies synthesis but also lowers the calcination temperature and reduces the time required to achieve crystallization, making it an appealing choice for large-scale production [10].

In traditional sol–gel synthesis, citric acid [11] is commonly used as a chelating agent to complex metal ions, facilitating the formation of a homogeneous gel. However, the novelty of this research lies in replacing citric acid with polyethylene glycol (PEG) with a molecular weight of 2000 (PEG-2000). This modification offers several advantages over conventional methods. PEG-2000, a polymeric chelating agent, acts as both a complexing agent and a fuel source for the combustion process, affecting the formation of the ferrite nanostructure [12]. PEG-2000's higher molecular weight compared to citric acid provides a more flexible and robust gel matrix, potentially improving the uniformity of the metal ion distribution and enhancing control over particle size during combustion [13].

2. Synthesis and characterization techniques

Nanoparticles were synthesized using high-purity chemical precursors, including iron nitrate nonahydrate ($Fe(NO_3)_3 9H_2O$), copper nitrate trihydrate ($Cu(NO_3)_2{\cdot}3H_2O$), and magnesium nitrate hexahydrate ($Mg(NO_3)_2{\cdot}6H_2O$), all obtained from LobaChemi, India [14]. Polyethylene glycol (PEG 2000), as chelating agent, sourced from Carl Roth GmbH, Germany, facilitating homogeneous metal ion dispersion and influencing nanoparticle dimensions and structure [15]. No additional chelating agents were employed. These nanoparticles were synthesized using a modified sol–gel autocombustion method [16], and the metal nitrates were mixed in a 1:1 nitrate: chelating agent ratio [17, 18] to maintain the appropriate balance of Mg^{2+}, Cu^{2+}, and Fe^{3+} ions for the targeted ferrite composition. The chemical precursors were dissolved in distilled water, and this mixture was continuously stirred to ensure uniformity. Following thorough mixing, the solution was subjected to a drying phase to eliminate moisture. The formatted xerogel was then placed in an oven pre-set to temperatures ranging from 250 °C to 300 °C. Within this temperature bracket, any residual moisture was driven off, and the xerogel underwent spontaneous combustion. This autoignition triggered a swift exothermic reaction, ultimately yielding a lightweight, porous material that was powdered into nanoparticles [16].

For each synthesized batch, the chemical composition and crystalline structure were examined using XRD analyses conducted on a PANalytical X'Pert Empyrean Series Bragg − Brentano powder diffractometer (United Kingdom) equipped with a Cu Kα radiation source ($\lambda = 1.5418$ Å) and operating over a 10–70° 2θ range with a scan increment of 0.013 for 2 s durations. ATR-FTIR spectra, covering a spectrum from 4000 to 370 cm^{-1}, were captured using a Bruker VERTEX 70v Fourier transform infrared spectrometer (Germany) with an ATR attachment at a resolution of 4 cm^{-1}. Magnetic properties at room temperature for all samples were quantified using a LakeShore Model 7407 (United States) vibrating sample magnetometer (VSM) under an argon atmosphere. RT Mössbauer spectroscopy measurements using a constant acceleration spectrometer with a 57Co source [19].

3. Results and discussion

3.1. X-ray diffraction studies

Figure 1 presents the x-ray diffraction patterns of magnesium-substituted copper nanoferrite samples ($Cu_{1-x}Mg_xFe_2O_4$ nanoparticles with $0.0 \leqslant x \leqslant 1.0$) synthesized using the sol–gel autocombustion method, with PEG-2000 as fuel. The characteristic peaks at 2θ angles (table 1) correspond to the (220), (311), (400), (511), and

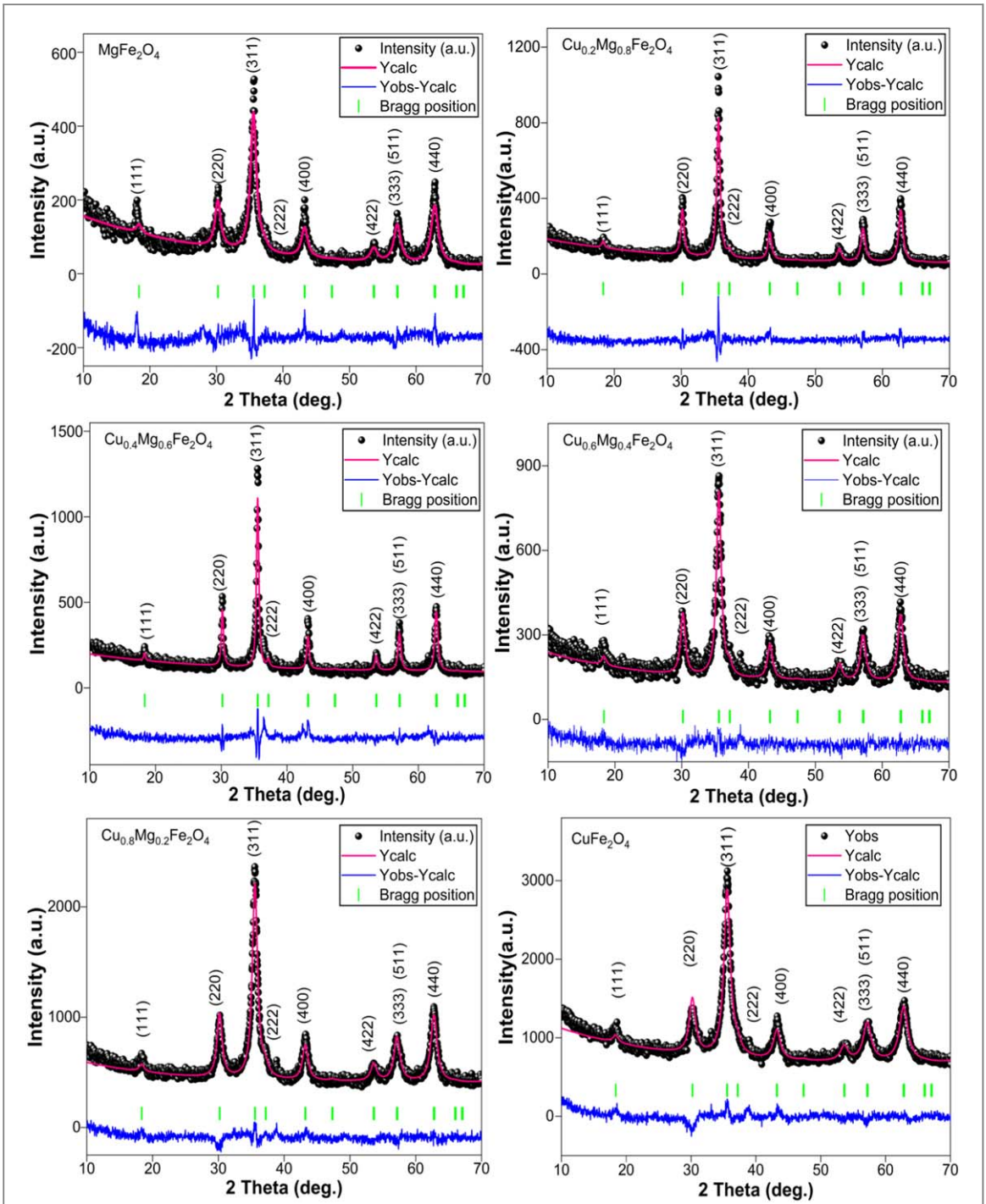

Figure 1. X-ray diffraction patterns of $Cu_{1-x}Mg_xFe_2O_4$ nanoparticles with $0.0 \leqslant x \leqslant 1.0$.

Table 1. Peak positions (2θ) of the reflection planes of the $Cu_{1-x}Mg_xFe_2O_4$.

Mg^{2+}(x)	2θ at (220)	2θ at (311)	2θ at (400)	2θ at (511)	2θ at (440)
0.0	30.17°	35.53°	43.19°	57.19°	62.73°
0.2	30.16°	35.52°	43.17°	57.10°	62.70°
0.4	30.16°	35.52°	43.18°	57.10°	62.71°
0.6	30.14°	35.51°	43.15°	57.07°	62.67°
0.8	30.14°	35.50°	43.14°	57.06°	62.66°
1.0	30.17°	35.54°	43.19°	57.13°	62.74°

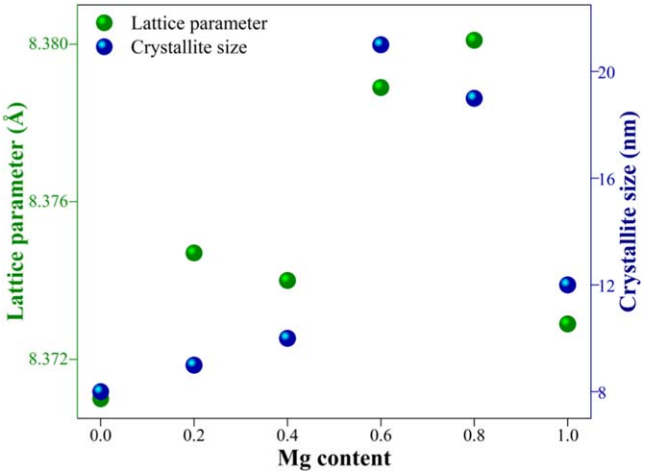

Figure 2. Crystallite size and lattice constant as a function of Mg content in $Cu_{1-x}Mg_xFe_2O_4$ nanoparticles.

(440) crystallographic planes, respectively. These peaks are consistent with the cubic spinel structure of the Fd3m space group [20, 21].

The absence of additional peaks indicates that no impurity phases are present. As the magnesium content increases, the diffraction peaks become sharper and narrower, suggesting an increase in particle size. This is likely due to the catalytic effect of magnesium, which leads to a higher temperature during the synthesis process [22].

The variation in the lattice constant as a function of magnesium content is depicted in figure 2. As the magnesium content increases, the lattice constant also increases. This is because copper ions, with a smaller ionic radius (0.72 Å for octahedral coordination), are replaced by magnesium ions, which have a larger ionic radius (0.86 Å for octahedral coordination), consistent with Vegard's law [23]. Williamson–Hall plot method was used to determine the crystallite size and internal lattice strains [16]. The variation in the crystallite size as a function of magnesium content is also shown in figure 2.

The substitution of Mg^{2+} leads to a systematic expansion of the lattice due to its larger ionic size, particularly when it replaces Fe^{3+} (0.645 Å for octahedral coordination) at the B-sites [24]. The lattice parameter (a) increases steadily from 8.3710 nm ($x = 0.0$) to 8.3801 nm ($x = 0.8$), reflecting the overall enlargement of the spinel lattice. Correspondingly, the tetrahedral bond length $d_{A\text{-}O}$ increases from 3.6247 nm to 3.6286 nm, and the octahedral bond length $d_{B\text{-}O}$ increases from 2.0927 nm to 2.0950 nm, indicating the structural adjustments required to accommodate the larger Mg^{2+} ions.

At lower substitution levels ($x \leqslant 0.4$), Mg^{2+} preferentially occupies the A-sites, replacing Cu^{2+} and causing a modest increase in $d_{A\text{-}O}$. The effect on $d_{B\text{-}O}$ is minimal in this range, as Fe^{3+} dominates the B-sites. However, as Mg content increases beyond ($x = 0.4$), a portion of Mg^{2+} migrates to the B-sites, competing with Fe^{3+} for occupancy. This redistribution contributes to a more significant increase in $d_{B\text{-}O}$, as the octahedral environment accommodates the larger Mg^{2+}.

Interestingly, at ($x = 1.0$), the lattice parameter $a = 8.3729$ nm and bond lengths $d_{A\text{-}O} = 3.6255$ nm, $d_{B\text{-}O} = 2.0932$ nm show a slight reduction compared to ($x = 0.8$). This deviation from the expected trend is likely due to increased lattice distortion and strain introduced by the full substitution of Cu^{2+} by Mg^{2+}, as well as a more uniform cation distribution across A- and B-sites. The accompanying increase in lattice strain ($\varepsilon = 0.011$) at ($x = 1.0$) supports this interpretation.

The crystallite size D exhibits a non-linear trend with Mg substitution, increasing significantly from 8 nm ($x = 0.0$) to 21 nm ($x = 0.6$), where lattice strain (ε) is minimized ($\varepsilon = 0.003$). This indicates that reduced internal stress facilitates crystal growth, resulting in larger crystallites. At higher Mg contents ($x = 0.8$) and ($x = 1.0$), the crystallite size decreases to 19 nm and 12 nm, respectively. This reduction is attributed to increased defects or strain, as evidenced by the rise in (ε) at these higher substitution levels. The interplay between strain and crystallite growth highlights the structural limitations imposed by excessive Mg substitution.

The bond lengths $d_{A\text{-}O}$ and $d_{B\text{-}O}$ and cation distribution directly influence the superexchange interactions [25], which direct the magnetic behavior of spinel ferrites [26]. The observed expansion in bond lengths with Mg substitution weakens the Fe-O-Fe superexchange pathways, potentially reducing magnetic ordering. Furthermore, the redistribution of Mg^{2+} ions between A- and B-sites affects the balance of magnetic and non-magnetic cations, altering the overall magnetic and electronic properties of the material. These structural changes are also reflected in the vibrational frequencies observed in FTIR spectra, where the shifts in ν_A and ν_B

Table 2. Structural parameters of $Cu_{1-x}Mg_xFe_2O_4$ nanoparticles: crystallite size (D), lattice parameter (a), lattice strain(ε), tetrahedral bond length d_{A-O} and octahedral bond length d_{B-O}.

$Cu_{1-x}Mg_xFe_2O_4$	FWHM	Crystallite size D, nm (±1)	Lattice constant a, nm (±0.0001)	Lattice strain, ε(±0.001)	d_{A-O} (nm) (±0.0001)	d_{B-O} (nm) (±0.0001)
x = 0.0	1.19461	7	8.3710	0.017	3.6247	2.0927
x = 0.2	0.94464	9	8.3747	0.012	3.6263	2.0936
x = 0.4	0.85110	10	8.3740	0.014	3.6260	2.0935
x = 0.6	0.35094	21	8.3789	0.003	3.6281	2.0947
x = 0.8	0.53012	19	8.3801	0.005	3.6286	2.0950
x = 1.0	1.06299	12	8.3729	0.011	3.6255	2.0932

are consistent with changes in bond lengths and cationic masses. All determined structural parameters of $Cu_{1-x}Mg_xFe_2O_4$ nanoparticles: crystallite size (D), lattice parameter (a), lattice strain(ε), tetrahedral bond length d_{A-O} and octahedral bond length d_{B-O} are summarized in table 2.

The cation distribution in the $Cu_{1-x}Mg_xFe_2O_4$ systems can be determined by analyzing the x-ray diffraction patterns. This study applied the Bertaut method [27] to calculate the cation distribution. This method involves selecting specific pairs of reflections based on the following equation:

$$\frac{I_{hkl}^{Obs}}{I_{h'k'l'}^{Obs}} = \frac{I_{hkl}^{Calc}}{I_{h'k'l'}^{Calc}} \tag{1}$$

Here, I_{OBS} and I_{CALC} represent the observed and calculated intensities for the (*hkl*) reflection, respectively. The intensity ratios of specific peak pairs in the XRD pattern of spinel structures, such as I_{220}/I_{400}, I_{220}/I_{422}, and I_{422}/I_{400}, are known to be sensitive to cation distribution [28]. The ratio of x-ray line intensities I_{220}/I_{440}, I_{220}/I_{400}, and I_{400}/I_{440} vary with the substitution of Mg ions, as shown in figure 3. As known, the spinel structure consists of two types of sites: tetrahedral (A) sites, typically occupied by divalent cations (in this case, Cu^{2+} and Mg^{2+}), and octahedral (B) sites, typically occupied by trivalent cations (Fe^{3+}), although some Cu^{2+} or Mg^{2+} may migrate to the B sites depending on the cation distribution. The ratio I_{220}/I_{440} is known to be sensitive to the distribution of divalent cations (Cu^{2+} and Mg^{2+}) between the tetrahedral (A) and octahedral (B) sites [29]. The values decrease from 0 to 0.4 Mg content, suggesting that Mg^{2+} starts to replace Cu^{2+} on the A sites. However, as Mg content increases further (up to 0.8), the ratio increases again, implying that some Mg^{2+} may be occupying B sites at higher substitution levels. The slight decrease at Mg = 1 suggests a more balanced distribution between the A and B sites. The ratio I_{400}/I_{440} generally reflects the occupancy of Fe^{3+} on octahedral (B) sites. A decreasing trend from Mg = 0 to Mg = 1 suggests that, as more Mg^{2+} replaces Cu^{2+} on the A sites, the Fe^{3+} occupancy on the B sites remains consistent or changes only slightly. However, at higher Mg content, more Mg^{2+} is likely migrating to the B sites. The ratio I_{220}/I_{400} provides a comparison between cations occupying A and B sites. The increasing trend from Mg = 0 to Mg = 1 indicates progressive substitution of Mg^{2+} for Cu^{2+} on the tetrahedral (A) sites. At higher Mg content (around 0.6 to 0.8), Mg^{2+} starts to occupy the octahedral (B) sites as well, as reflected by the higher values [30].

As seen in figure 3, at lower Mg substitution levels ($x \leqslant 0.4$), Mg^{2+} primarily occupies the tetrahedral (A) sites, replacing Cu^{2+}. As the Mg content increases beyond x = 0.4, a portion of Mg^{2+} begins to migrate to the octahedral (B) sites, competing with Fe^{3+} for occupancy. This explains the increase in I_{220}/I_{440} and I_{220}/I_{400} at higher Mg content (x = 0.6 to 0.8). At Mg = 1, the distribution appears more balanced, with Mg^{2+} occupying both tetrahedral (A) and octahedral (B) sites. This pattern suggests that Mg^{2+} ions prefer tetrahedral sites at lower substitution levels but increasingly occupy octahedral sites as their concentration increases, which is typical behavior for divalent cations in spinel ferrites [31]. The cation distribution for each Mg^{2+} content, along with the site preferences of cations between A-sites and B-sites, indicating the fraction of Cu^{2+} and Fe^{3+} ions at each site, is provided in table 3.

3.2. Fourier transform infrared spectroscopy (FTIR)

Figure 4 shows the results from Fourier transform infrared (FTIR) spectroscopy, which detects specific vibrational modes within the material. Two clear peaks are observed at 370–393 cm^{-1} and 538–543 cm^{-1}, corresponding to the stretching vibrations of the Fe-O bonds located in tetrahedral and octahedral sites, respectively [32]. These peaks confirm the successful formation of the spinel structure, as these vibrations are characteristic of this phase.

The variation in the vibrational frequencies of the tetrahedral (υ_A) and octahedral (υ_B) sites with Mg substitution does not follow a simple, predictable pattern. Figures 5(a) and (b) illustrate how the changes in these bond lengths and cationic masses affect the vibrational frequencies. Typically, the frequencies of these vibrational bands are influenced by two main factors: bond lengths (R_A for the tetrahedral and R_B for the

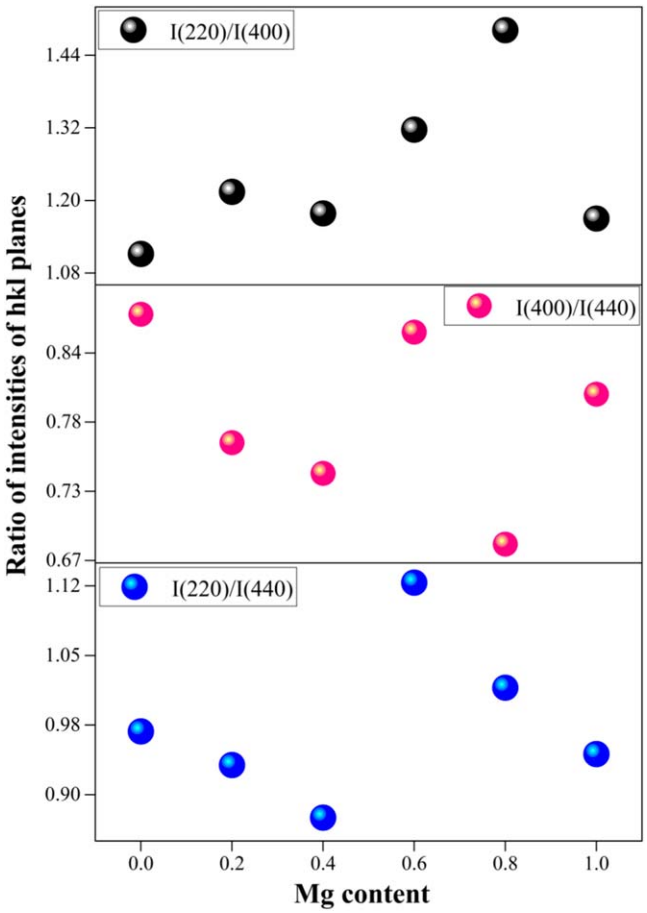

Figure 3. Variation of crystal plane intensities I_{220}/I_{440}, I_{220}/I_{400}, and I_{400}/I_{440} versus Mg content in $Cu_{1-x}Mg_xFe_2O_4$ nanoparticles.

Table 3. Cation distribution data from XRD Rietveld fitting for $Cu_{1-x}Mg_xFe_2O_4$ systems.

Composition	Cation distribution (XRD)	Vibrational frequency band	
		ν_A	ν_B
$CuFe_2O_4$	$(Cu_{0.86}Fe_{0.137})_A[Cu_{0.137}Fe_{1.863}]_B$	370	538
$Cu_{0.8}Mg_{0.2}Fe_2O_4$	$(Cu_{0.78}Mg_{0.10}Fe_{0.10})_A\,[Cu_{0.02}Mg_{0.1}Fe_{1.88}]_B$	393	540
$Cu_{0.6}Mg_{0.4}Fe_2O_4$	$(Cu_{0.5}Mg_{0.20}Fe_{0.3})_A\,[Cu_{0.05}Mg_{0.2}Fe_{1.75}]_B$	392	539
$Cu_{0.4}Mg_{0.6}Fe_2O_4$	$(Cu_{0.2}Mg_{0.25}Fe_{0.55})_A\,[Cu_{0.2}Mg_{0.35}Fe_{1.45}]_B$	370	536
$Cu_{0.2}Mg_{0.8}Fe_2O_4$	$(Cu_{0.1}Mg_{0.3}Fe_{0.55})_A\,[Cu_{0.1}Mg_{0.45}Fe_{1.45}]_B$	374	540
$MgFe_2O_4$	$(Mg_{0.831}Fe_{0.169})_A[Mg_{0.169}Fe_{1.831}]_B$	376	542

octahedral sites) and the masses of the cations (M_A and M_B) at these sites. This is because the vibrational frequency is inversely proportional to both the bond length and the cationic mass. A longer bond or a heavier cation would generally result in a lower vibrational frequency. Based on this principle, when Mg^{2+} substitutes for Cu^{2+} at the A-site (tetrahedral), one would expect a steady decrease in υ_A because Mg^{2+} has a smaller cationic mass compared to Cu^{2+}. However, the actual experimental data show that the decrease in υ_A is not consistent with this expectation. This discrepancy suggests that changes in the bond length R_A (the distance between the cations and oxygen in the tetrahedral site) play a larger role in determining the vibrational frequency than the mass of the substituting cations alone.

In the case of the octahedral site (υ_B), the variation in the vibrational frequency can similarly be attributed to changes in the bond length R_B and the cationic mass M_B at the B-site. At lower Mg^{2+} concentrations ($x = 0.2$ and $x = 0.4$), the observed shifts in υ_B align with what would be expected from changes in M_B, indicating that cationic mass is the dominant factor. However, for higher Mg^{2+} concentrations ($x \geqslant 0.4$), the variation in υ_B cannot be fully explained by changes in M_B or R_B alone. This suggests that other structural factors, such as the redistribution of cations between the A- and B-sites, may be influencing vibrational behavior. The random distribution of Mg^{2+} and Cu^{2+} between the tetrahedral and octahedral sites in $Cu_{1-x}Mg_xFe_2O_4$ is supported by

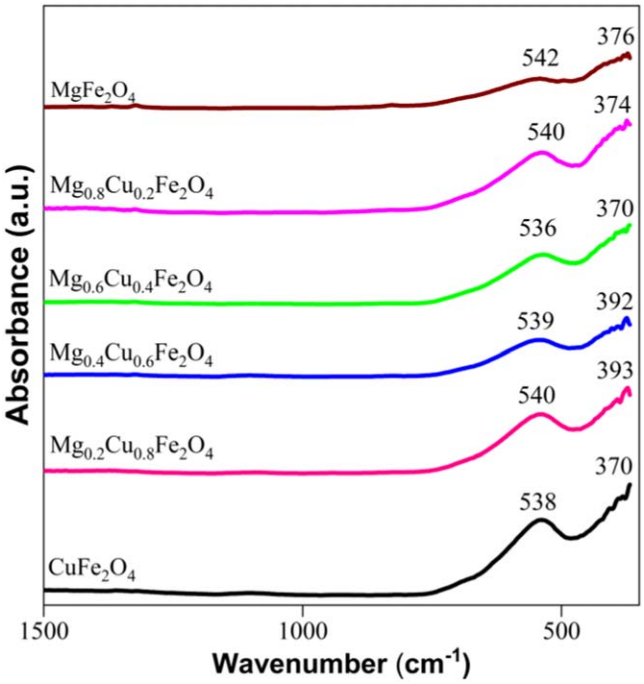

Figure 4. FTIR spectra of $Cu_{1-x}Mg_xFe_2O_4$ nanoparticles.

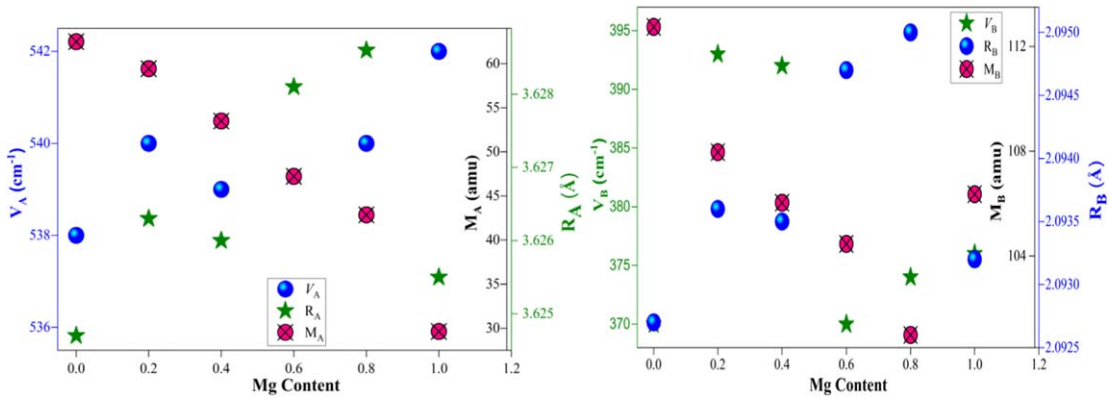

Figure 5. Variation of tetrahedral vibrational band υ_A and octahedral vibrational band υ_B along with bond lengths (R_A and R_B) and cationic masses (M_A and M_B) with Mg substitution.

the fact that both υ_A and υ_B are affected by the substitution. This indicates that Mg^{2+} substitution influences not just one type of site but affects the overall cation distribution within the spinel structure, leading to complex variations in vibrational frequencies [33].

The elastic constants, including the tetrahedral (K_T), octahedral (K_O), and average (K) force constants for the $Cu_{1-x}Mg_xFe_2O_4$ nanoparticles, were determined from the calculated vibrational frequency values [30] and are presented in table 4. Figure 6 illustrates the variation in these force constants as a function of Mg^{2+} ion concentration in the $Cu_{1-x}Mg_xFe_2O_4$ system [34]. Additionally, the elastic moduli, such as the bulk modulus (B), Young's modulus (Y), rigidity modulus (G), and Poisson's ratio (P), were also computed and are shown in table 4.

As the Mg content increases in the $Cu_{1-x}Mg_xFe_2O_4$ system, a general decrease is observed in both the force constants and elastic moduli. This trend suggests the material becomes progressively softer and less resistant to mechanical deformation. The decrease in force constants, such as K_T and K_O, reflects the weakening of bonding within the crystal lattice, particularly between the cations and oxygen ions. The reduced elastic moduli further support this conclusion, indicating that the material's structural rigidity declines with higher Mg^{2+} substitution. The reduction in the elastic properties is accompanied by a corresponding decrease in sound velocities and the Debye temperature [35]. This decrease suggests that the material's internal bonding structure weakens as Mg^{2+}

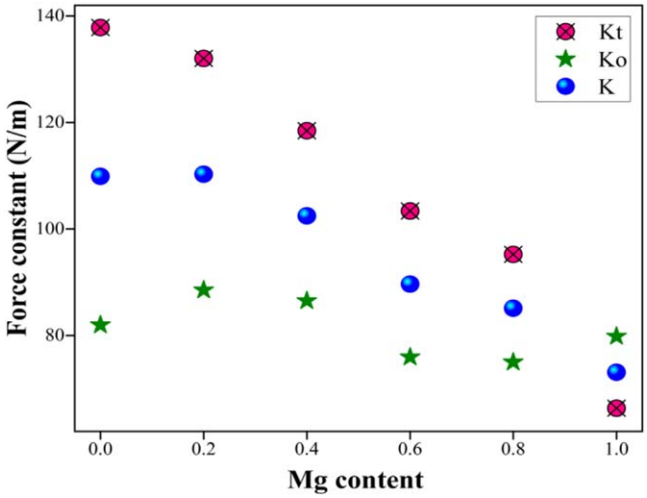

Figure 6. Force constant as a function of Mg ions concentration $Cu_{1-x}Mg_xFe_2O_4$ system.

Table 4. Force constants and elastic constants of $Cu_{1-x}Mg_xFe_2O_4$ samples.

$Cu_{1-x}Mg_xFe_2O_4$ x	K_T	K_O	B	Y	G	P
	N/m (±1)			GPa (±0.01)		
0.0	138	82	82.64	111.58	43.76	0.307
0.2	128	89	79.78	109.79	43.20	0.297
0.4	118	86	73.59	103.09	40.70	0.287
06	108	74	64.25	91.71	36.33	0.277
0.8	99	72	58.89	85.56	34.01	0.267
1	66	80	49.61	73.02	29.10	0.260

ions replace more Cu^{2+} ions. The Debye temperature, which is linked to lattice vibrations and the strength of atomic interactions, provides further evidence that the substitution of magnesium weakens the overall bonding network within the spinel structure [36].

3.3. Mossbauer studies

Figure 7 displays the room-temperature Mössbauer spectrum of the spinel system $Cu_{1-x}Mg_xFe_2O_4$ for $0.0 \leqslant x \leqslant 1.0$, using the ^{57}Fe isotope. The Mössbauer spectrum provides valuable information about the hyperfine interactions within the material, including the magnetic environment of the Fe ions in both the tetrahedral (A-site) and octahedral (B-site) positions. The main Mössbauer parameters, such as the isomer shift (I_S), quadrupole splitting (Q_S), and hyperfine magnetic field (H), are summarized in table 5. These parameters help characterize the electronic and magnetic states of the iron ions. The isomer shift indicates the oxidation state of the iron, while the quadrupole splitting reflects the symmetry of the local electric field around the iron nuclei. The hyperfine magnetic field provides insight into the magnetic ordering of the system. As the Mg^{2+} concentration increases ($0.0 \leqslant x \leqslant 1.0$), changes in these Mössbauer parameters are observed, reflecting the influence of Mg^{2+} substitution on the local environment of the Fe ions and the overall magnetic properties of the spinel system.

Each Mössbauer spectrum in figure 7 shows multiple magnetically ordered sextets coexisting with a paramagnetic doublet, whose intensity varies with the magnesium concentration. The paramagnetic doublet arises due to superparamagnetic relaxation, which is influenced by the small particle size and the effect of temperature. This leads to background distortion and the appearance of the doublet. In interpreting the Mössbauer spectra, it's important to consider the superexchange interaction between Fe ions mediated by oxygen. This interaction weakens as the distance between magnetic ions increases and the Fe–O–Fe bond angle narrows from 180° to 90°. In $CuFe_2O_4$, the antiferromagnetic interaction between Fe ions at the A and B sites (Fe (A)–O–Fe(B)) is stronger than the ferromagnetic interactions within the A–A and B–B sites. Since each iron ion at the A site is surrounded by 12 octahedral ions, substituting Mg^{2+} at the B site does not significantly alter the overall interaction, resulting in little change to the hyperfine field (H) at the A site. However, at the B site, iron ions are connected to only six A-site neighbors. Replacing Fe^{3+} at the A site with Cu^{2+} or Mg^{2+} ions alters the

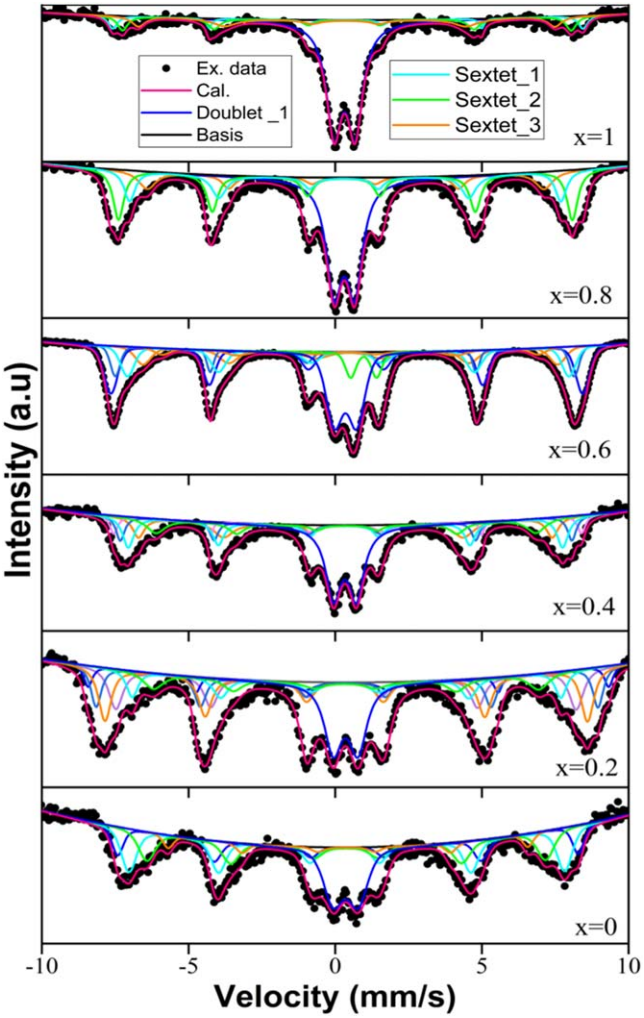

Figure 7. RT Mössbauer spectra of ^{57}Fe in $Cu_{1-x}Mg_xFe_2O_4$ system.

superexchange interaction, broadening the subspectral lines of Fe(B) ions due to the varying environments in the A sublattice. This leads to more resonance lines and broader subspectral features in the Mössbauer spectrum [37].

As in table 5, more than two subspectra were identified—one for A-site Fe ions and several for B-site Fe ions. In addition, the nanoscale samples show partial paramagnetism, indicated by a central quadrupole doublet resulting from superparamagnetic relaxation. This doublet, superimposed on magnetically split sextets, reflects the coexistence of superparamagnetic and ferromagnetic particles. The broad linewidth (FWHM) and reduced internal magnetic field in nanosamples suggest a shift from typical magnetic behavior caused by the small particle size. Lower isomer shift values at the A sites, compared to the B sites, are due to stronger Fe^{3+}–O^{2-} bonding at the A site, leading to greater orbital overlap and higher covalency [38].

In nanoscale materials, superparamagnetism occurs when thermal energy causes magnetic moments to fluctuate rapidly, preventing the observation of fixed magnetization. This relaxation behavior results in the absence of Zeeman splitting in smaller particles. In systems like Cu–Mg ferrite, random distribution of Mg^{2+} ions in the A-site coordination sphere leads to variations in Fe^{3+} configurations at B sites, creating differences in the hyperfine field, known as super transferred hyperfine interaction [39]. These differences contribute to the broadening of the Mössbauer spectral lines. The appearance of a second doublet in the sample with $x = 0.6x = 0.6x = 0.6$ is due to nonmagnetic substitution, as indicated by XRD analysis, which shows larger crystallites. In this case, iron ions are surrounded by more nonmagnetic neighbors, leading to a paramagnetic doublet (Doublet_2). Surface effects, particle size, and cation distribution significantly influence the Mössbauer parameters in the $Cu_{1-x}Mg_xFe_2O_4$ system.

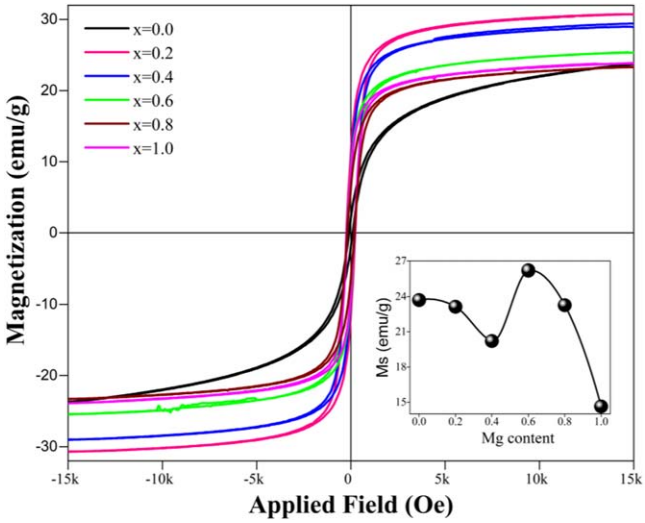

Figure 8. Hysteresis loops of $Cu_{1-x}Mg_xFe_2O_4$ system.

Table 5. RT Mössbauer Spectra Parameters of ^{57}Fe in $Cu_{1-x}Mg_xFe_2O_4$ system.

Sample $Cu_{1-x}Mg_xFe_2O_4$	Component	Is, mm/s	Qs, mm/s	H, kOe	S, %	G, mm/s	Chi2
	Sextet_1	0.3876	0.0105	487.62	16.87	0.4629	
	Sextet_2	0.3188	0.0694	461.41	29.54	0.6109	
0.0	Sextet_3	0.3331	0.0040	422.28	22.35	0.6717	1.462
	Sextet_4	0.3676	0.0600	380.86	6.89	0.4155	
	Doublet_1	0.3143	0.8367	—	22.34	0.7982	
	Sextet_1	0.4303	0.0420	551.27	6.75	0.3458	
	Sextet_2	0.3812	0.0487	531.35	14.24	0.4235	
0.2	Sextet_3	0.3560	0.0422	510.91	22.21	0.5158	1.417
	Sextet_4	0.3396	0.0617	487.48	17.54	0.5701	
	Sextet_5	0.3581	0.0621	453.79	11.50	0.4553	
	Sextet_6	0.3518	0.0467	408.17	9.71	0.7981	
	Doublet_1	0.3545	0.8393	—	18.05	0.7215	
	Sextet_1	0.3989	0.0474	495.19	8.46	0.3205	
	Sextet_2	0.3520	0.0411	478.12	12.87	0.3539	
0.4	Sextet_3	0.3294	0.0427	459.89	19.69	0.4566	1.432
	Sextet_4	0.3152	0.0685	438.05	16.30	0.4732	
	Sextet_5	0.3832	−0.0270	402.50	13.56	0.7740	
	Doublet_1	0.3317	0.7799	—	29.12	0.6325	
	Sextet_1	0.3836	0.0262	499.52	25.70	0.5600	
	Sextet_2	0.2995	0.0540	485.82	11.04	0.3941	
0.6	Sextet_3	0.4134	0.0603	467.44	17.60	0.5551	3.104
	Sextet_4	0.4924	0.0505	438.98	12.47	0.6318	
	Sextet_5	0.4418	0.1362	398.38	4.77	0.6116	
	Doublet_1D	0.9710	0.8843	—	5.22	0.4244	
	oublet_2	0.3516	0.7486	—	23.21	0.6662	
	Sextet_1	0.3738	0.0414	501.28	14.87	0.3928	
	Sextet_2	0.3232	0.0651	481.88	21.16	0.4425	
0.8	Sextet_3	0.3248	0.0544	458.92	15.36	0.4768	1.483
	Sextet_4	0.3381	0.0861	429.66	9.37	0.4473	
	Sextet_5	0.3629	0.0970	397.12	4.97	0.3560	
	Doublet_1	0.3143	0.6989	—	34.27	0.6387	
	Sextet_1	0.3918	0.0858	497.95	8.21	0.3681	
	Sextet_2	0.3513	0.0963	474.87	12.89	0.4157	
1.0	Sextet_3	0.3698	0.0478	440.73	14.13	0.5383	1.077
	Doublet_1	0.3200	0.7173	—	64.76	0.6322	

Table 6. Magnetic properties of parameters of $Cu_{1-x}Mg_xFe_2O_4$ system.

x	M_S (emu/g)	M_R (emu/g)	H_C (Oe)	T(K)	M_R/M_S	t (nm)	t′ (nm)	θ_C(degree)
0.0	23.71	2.03	94.6	713	0.0856	0.452	0.516	53.64
0.2	23.14	1.73	99.3	670	0.0747	0.479	0.541	51.28
0.4	20.22	1.13	67.3	686	0.0558	0.613	0.709	53.50
0.6	26.21	1.56	99.2	631	0.0595	0.540	0.571	32.27
0.8	23.27	1.36	119	780	0.0584	1.621	2.020	58.47
1	14.64	0.69	89.7	640	0.0471	0.395	0.424	21.44

3.4. Magnetic studies

Figure 8 presents the room temperature hysteresis curves of $Cu_{1-x}Mg_xFe_2O_4$ samples synthesized by the modified combustion method. In these ferrites, the overall magnetization results from the interplay between the tetrahedral and octahedral sublattices [40]. The magnetization is primarily influenced by the redistribution of iron ions between these sublattices, as shown in the cation distribution in table 3.

As the level of magnesium substitution increases (table 6), the saturation magnetization (M_s) exhibits a non-monotonic trend, reaching a maximum value of 26.21 emu g^{-1} at $x = 0.6$ before decreasing. This behavior aligns with previously reported findings. Notably, Akter *et al* [41] observed an M_s value of 27 emu g^{-1} for a $Cu_{0.5}Mg_{0.5}Fe_2O_4$ sample, while Chandra Devsharma *et al* [42] reported M_s values of 22 emu g^{-1} for $CuFe_2O_4$ and 20 emu g^{-1} for $MgFe_2O_4$. This behavior reflects complex cation interactions and structural changes affecting Fe^{3+} ions, the primary source of magnetization. The spin canting angle (θc) varies significantly with magnesium content. A reduction in crystallite size, coupled with an increase in the spin canting angle, results in a decline in saturation magnetization (M_s) [43, 44]. For pure $CuFe_2O_4$, θc is about 53.65°, indicating notable spin misalignment due to structural distortions [45]. As Mg content rises to $x = 0.6$, θc decreases sharply to 32.28°, suggesting better spin alignment and stronger magnetic interactions, as evidenced by the increased M_s. However, at $x = 0.8$, the canting angle increases to 58.48°, reflecting higher spin disorder, likely due to nonmagnetic Mg^{2+} weakening magnetic interactions [46]. The spin-canting analysis reveals that Mg substitution profoundly affects magnetic properties. Lower Mg content ($x = 0.2$) slightly improves spin alignment, while higher levels ($x = 0.4$, $x = 0.8$) increase spin disorder. The composition $x = 0.6$ stands out for its reduced canting angle and higher saturation magnetization, suggesting this is the optimal composition for magnetic performance in the series. However, further increases in Mg content diminish these magnetic properties due to weakened interactions.

4. Conclusions

In this study, a system of magnesium-substituted copper ferrites was developed using the sol–gel autocombustion method with polyethylene glycol-2000 (PEG-2000) as fuel. The investigation focused on the effect of replacing the chelating agent on the structural, elastic, and magnetic properties of the material. All synthesized systems were identified as single-phase cubic spinel with the space group Fd3m, with no impurity phases detected. It was demonstrated that using PEG-2000 as both fuel and chelating agent led to a significant reduction in particle size to 8–21 nm. With an increase in magnesium ion content, the lattice constant increased due to substituting smaller ions with larger ones. FTIR studies confirmed the formation of a single-phase spinel, as evidenced by characteristic spinel peaks, with no additional peaks indicating impurity phases. As the magnesium ion content increased, the elastic constants gradually rose. The observed increase in Debye temperature with higher magnesium concentration suggests a strengthening of the material's structure upon substitution.

The Mössbauer spectroscopy studies of magnesium-substituted copper spinel reveal important insights into the material's magnetic and structural properties. The presence of multiple magnetically ordered sextets and a paramagnetic doublet indicates a complex interaction between ferromagnetic and superparamagnetic phases as Mg^{2+} concentration varies. Key findings include changes in isomer shift, quadrupole splitting, and hyperfine magnetic fields, reflecting the local environment of iron ions influenced by Mg^{2+} substitution. The broadening of spectral lines suggests that particle size and cation distribution lead to super-transferred hyperfine interactions. Overall, Mössbauer's studies highlight the significant role of cation distribution and superexchange interactions in determining the magnetic behavior of the $Cu_{1-x}Mg_xFe_2O_4$ spinel system, contributing to its potential applications.

The magnetic properties of samples exhibit notable trends. The saturation magnetization M_S generally decreases with increasing magnesium content, except for the ($x = 0.6$) sample, which shows the highest M_S value of 26.21 emu g^{-1}. The spin canting angle θ_C varies significantly, with the highest canting observed in the

(x = 0.8) sample (58.47°), suggesting more significant spin misalignment in this system. The smallest canting angle is found in the (x = 1.0) sample (21.44°), indicating better alignment of magnetic moments. This variation in spin canting and magnetic properties can be attributed to the structural changes induced by magnesium substitution. The composition x = 0.6 stands out for its reduced canting angle and higher saturation magnetization, suggesting this is the optimal composition for magnetic performance in the series.

Acknowledgments

The authors acknowledge the financial support provided by the Polish National Agency for Academic Exchange (Narodowa Agencja Wymiany Akademickiej). Additionally, the authors are grateful for the funding received from the Ministry of Education and Science of Ukraine (Project Number 0124U001654).

Data availability statement

All data that support the findings of this study are included within the article (and any supplementary files).

Funding

This work was supported by the Narodowa Agencja Wymiany Akademickiej (Grant Ulam NAWA: BPN/ULM/2022/1/00093) and partly supported by a grant 0124U001654 of the Ministry of Education and Science of Ukraine.

ORCID iDs

J Mazurenko https://orcid.org/0000-0002-8446-5280
Sijo A K https://orcid.org/0000-0002-1478-2088
J M Michalik https://orcid.org/0000-0002-6019-3532
Ł Gondek https://orcid.org/0000-0002-4149-7944
E Szostak https://orcid.org/0000-0002-5576-2120
Żywczak A https://orcid.org/0000-0001-9554-3742
V Moklyak https://orcid.org/0000-0002-0174-7718

References

[1] Askarzadeh N and Shokrollahi H 2024 A review on synthesis, characterization and properties of lithium ferrites *Results Chem.* **10** 101679
[2] Channagoudra G, Saw A K and Dayal V 2021 Role of structure and cation distribution on magnetic and electrical properties in inverse spinel copper ferrite *J. Phys. Chem. Solids* **154** 110086
[3] Uddin M J and Jeong Y-K 2022 Application of magnesium ferrite nanomaterials for adsorptive removal of arsenic from water: effects of Mg and Fe ratio *Chemosphere* **307** 135817
[4] Bhandare S V, Kumar R, Anupama A V, Mishra M, Vijaya Kumar R, Jali V M and Sahoo B 2020 Effect of Mg-substitution in Co–Ni-Ferrites: cation distribution and magnetic properties *Mater. Chem. Phys.* **251** 123081
[5] Priyadharshini P and Pushpanathan K 2023 Synthesis of Ce-doped $NiFe_2O_4$ nanoparticles and their structural, optical, and magnetic properties *Chem. Phys. Impact* **6** 100201
[6] Soufi A, Hajjaoui H, Elmoubarki R, Abdennouri M, Qourzal S and Barka N 2021 Spinel ferrites nanoparticles: synthesis methods and application in heterogeneous Fenton oxidation of organic pollutants—a review *Appl. Surf. Sci. Adv.* **6** 100145
[7] Salih S J and Mahmood W M 2023 Review on magnetic spinel ferrite (MFe_2O_4) nanoparticles: from synthesis to application *Heliyon* **9** e16601
[8] Nyabadza A, McCarthy É, Makhesana M, Heidarinassab S, Plouze A, Vazquez M and Brabazon D 2023 A review of physical, chemical and biological synthesis methods of bimetallic nanoparticles and applications in sensing, water treatment, biomedicine, catalysis and hydrogen storage *Adv. Colloid Interface Sci.* **321** 103010
[9] Arifuzzaman H M B, Harun-Or-Rashid M and R M L 2021 Structural and magnetic properties of nanocrystalline $Ni_{0.7-x}Cu_xCd_{0.3}Fe_2O_4$ prepared through Sol–gel method *Mater. Charact.* **171** 110810
[10] Shirsath S E, Jadhav S S, Mane M L and Li S 2016 *Ferrites Obtained by Sol–Gel Method* ed L Klein, M Aparicio and A Jitianu (Handbook of Sol-Gel Science and Technology) pp 125–1
[11] Kaykan L S *et al* 2022 Influence of the preparation method and aluminum ion substitution on the structure and electrical properties of lithium–iron ferrites *Appl. Nanosci.* **12** 503–11
[12] Hussein S I, Elkady A S, Rashad M M, Mostafa A G and Megahid R M 2015 Structural and magnetic properties of magnesium ferrite nanoparticles prepared via EDTA-based sol–gel reaction *J. Magn. Magn. Mater.* **379** 9–15
[13] Díez A G, Rincón-Iglesias M, Lanceros-Méndez S, Reguera J and Lizundia E 2022 Multicomponent magnetic nanoparticle engineering: the role of structure-property relationship in advanced applications *Mater. Today Chem.* **26** 101220

[14] Mazurenko J, Kaykan L, Bandura K, Vyshnevskyi O, Moiseienko M, Kuzyshyn M and Ostapovych N 2024 Analysis of the structural, morphological, and elastic properties of nanosized $CuFe_2O_4$ spinel synthesized via sol-gel self-combustion method *Phys. Chem. Solid State* **25** 380–90
[15] Shi L, Zhang J, Zhao M, Tang S, Cheng X, Zhang W, Li W, Liu X, Peng H and Wang Q 2021 Effects of polyethylene glycol on the surface of nanoparticles for targeted drug delivery *Nanoscale* **13** 10748–64
[16] Mazurenko J, Kaykan L, Michalik J M, Sikora M, Szostak E, Vyshnevskyi O, Bandura K and Turovska L 2024 Enhanced synthesis of copper ferrite magnetic nanoparticles via polymer-assisted sol-gel autocombustion method for magnetic hyperthermia applications *J. Nano Res.* **84** 95–116
[17] Sijo A K, Lakshmi N, Venugopalan K, Dutta D P and Jain V K 2015 Effect of fuel to oxidizer ratio on structural and magnetic properties of ZnCrFeO4 nanopowder *Adv. Porous Mater.* **2** 189–91
[18] Sijo A K 2017 Influence of fuel-nitrate ratio on the structural and magnetic properties of Fe and Cr based spinels prepared by solution self combustion method *J. Magn. Magn. Mater.* **441** 672–7
[19] Pęczkowski P, Szostak E, Pocheć E, Michalik J M, Piętosa J, Tahraoui T, Łuszczek M and Gondek Ł 2023 Biocompatibility and potential functionality of lanthanum-substituted cobalt ferrite spinels *J. Alloys Compd.* **966** 171433
[20] Mounkachi O, Hamedoun M, Belaiche M, Benyoussef A, Masrour R, El Moussaoui H and Sajieddine M 2012 Synthesis and magnetic properties of ferrites spinels $MgxCu_{1-x}Fe_2O_4$ *Physica* B **407** 27–32
[21] Sijo A K 2017 Magnetic and structural properties of $CoCrxFe_{2-x}O_4$ spinels prepared by solution self combustion method *Ceram. Int.* **43** 2288–90
[22] Kutty P V M and Dasgupta S 2013 Low temperature synthesis of nanocrystalline magnesium aluminate spinel by a soft chemical method *Ceram. Int.* **39** 7891–4
[23] Brown I D 2009 Recent developments in the methods and applications of the bond valence model *Chem. Rev.* **109** 6858–919
[24] Murugesan C, Sathyamoorthy B and Chandrasekaran G 2015 Structural, dielectric and magnetic properties of Gd substituted manganese ferrite nanoparticles *Phys. Scr.* **90** 085809
[25] Thanh T D, Nha T T N, Giang T T H, Nam P H, Toan D N, Khan D T, Manh D H and Phong P T 2024 Structural, optical, magnetic properties and energy-band structure of MFe2O4 (M = Co, Fe, Mn) nanoferrites prepared by co-precipitation technique *RSC Adv.* **14** 23645–60
[26] Sharma R, Thakur P, Kumar M, Barman P B, Sharma P and Sharma V 2017 Enhancement in A-B superexchange interaction with Mn^{2+} substitution in Mg-Zn ferrites as a heating source in hyperthermia applications *Ceram. Int.* **43** 13661–9
[27] Neupane D, Wang L, Adhikari H, Alam J and Mishra S R 2016 Influence of Al^{3+} doping on structural and magnetic properties of $CoFe_{2-x}Al_xO_4$ ferrite nanoparticles *J. Alloys Compd.* **688** 413–21
[28] Wei Q, Li J, Chen Y and Han Y 2002 Cation distribution in $Ni_xMn_{1-x}Fe_2O_4$ ferrites *Mater. Chem. Phys.* **74** 340–3
[29] Bindu K, Ajith K M and Nagaraja H S 2019 Influence of cations on the dielectric properties of spinel structured nanoferrites *Mater. Res. Express* **6** 04501
[30] Kagdi A R, Solanki N P, Carvalho F E, Meena S S, Bhatt P, Pullar R C and Jotania R B 2018 Influence of Mg substitution on structural, magnetic and dielectric properties of x-type barium-zinc hexaferrites $Ba_2Zn_{2-x}Mg_xFe_{28}O_{46}$ *J. Alloys Compd.* **741** 377–91
[31] Adeela N, Maaz K, Khan U, Karim S, Nisar A, Ahmad M, Ali G, Han X F, Duan J L and Liu J 2015 Influence of manganese substitution on structural and magnetic properties of $CoFe_2O_4$ nanoparticles *J. Alloys Compd.* **639** 533–40
[32] Mohapatra J, Mitra A, Tyagi H, Bahadur D and Aslam M 2015 Iron oxide nanorods as high-performance magnetic resonance imaging contrast agents *Nanoscale* **7** 9174–84
[33] Watawe S C, Sutar B D, Sarwade B D and Chougule B K 2001 Infrared studies of some mixed Li–Co ferrites *Int. J. Inorg. Mater.* **3** 819–23
[34] Yousaf M, Nazir S, Hayat Q, Akhtar M N, Akbar M, Lu Y, Noor A, Zhang J M, Yousaf Shah M A K and Wang B 2021 Magneto-optical properties and physical characteristics of M-type hexagonal ferrite ($Ba_{1-x}Ca_xFe_{11.4}Al_{0.6}O_{19}$) nanoparticles (NPs) *Ceram. Int.* **47** 11668–76
[35] Ganeshan S, Shang S L, Wang Y and Liu Z-K 2009 Effect of alloying elements on the elastic properties of Mg from first-principles calculations *Acta Mater.* **57** 3876–84
[36] Sujatha C, Venugopal Reddy K, Sowri Babu K, Rama Chandra Reddy A and Rao K H 2012 Effects of heat treatment conditions on the structural and magnetic properties of MgCuZn nano ferrite *Ceram. Int.* **38** 5813–20
[37] Sijo A K, Jha V K, Kaykan L S and Dutta D P 2020 Structure and cation distribution in superparamagnetic $NiCrFeO_4$ nanoparticles using mössbauer study *J. Magn. Magn. Mater.* **497** 166047
[38] Moya C, Iglesias-Freire Ó, Batlle X, Labarta A and Asenjo A 2015 Superparamagnetic versus blocked states in aggregates of $Fe_{3-x}O_4$ nanoparticles studied by MFM *Nanoscale* **7** 17764–70
[39] Issa B, Obaidat I M, Albiss B A and Haik Y 2013 Magnetic nanoparticles: surface effects and properties related to biomedicine applications *Int. J. Mol. Sci.* **14** 21266–305
[40] Manohar A, Chintagumpala K and Kim K H 2021 Mixed Zn–Ni spinel ferrites: Structure, magnetic hyperthermia and photocatalytic properties *Ceram. Int.* **47** 7052–61
[41] Akter S, Khan M N I, Ferdous F, Das H N and Syed I M 2022 Analysis of the influence of trivalent Cr3+ doping on the structural and electromagnetic properties of Cu0.5Mg0.5CrxFe2−xO4 nanoferrites *AIP Adv.* **12** 095015
[42] Chandra Devsharma S, Rahman M L, Hossain M J, Biswas B, Ahmed M F and Sharmin N 2024 Elucidation of structural, electromagnetic, and optical properties of Cu–Mg ferrite nanoparticles *Heliyon* **10** e33578
[43] Amer M A, Meaz T, Yehia M, Attalah S S and Fakhry F 2015 Characterization, structural and magnetic properties of the as-prepared Mg-substituted Cu-nanoferrites *J. Alloys Compd.* **633** 448–55
[44] Gadkari A B, Shinde T J and Vasambekar P N 2010 Magnetic properties of rare earth ion (Sm3+) added nanocrystalline Mg–Cd ferrites, prepared by oxalate co-precipitation method *J. Magn. Magn. Mater.* **322** 3823–7
[45] Benamara N, Setifi Z, Yang C-I, Bernès S, Geiger D K, Kürkçüoğlu G S, Setifi F and Reedijk J 2021 Coexistence of spin canting and metamagnetism in a one-dimensional Mn(II) compound bridged by alternating double end-to-end and double end-on azido ligands and the analog Co(II) compound *Magnetochemistry* **7** 50
[46] Hammad T M, Kuhn S, Amsha A A, Hejazy N K and Hempelmann R 2020 Comprehensive study of the impact of Mg2+ doping on optical, structural, and magnetic properties of copper nanoferrites *J. Supercond. Nov. Magn.* **33** 3065–75